

A mixed 8-node hexahedral element based on the Hu-Washizu principle and the field extrapolation technique

Yung-I Chen[†]

Bureau of High Speed Rail, Ministry of Transportation and Communications, 13F, No. 7, Sec. 2, Sianmin Blvd., Banchiao City, Taipei County, 220, Taiwan, R.O.C.

Guan-Yuan Wu[‡]

Department of Fire Science, Central Police University, No. 56, Shu Jen Road, Ta Kang, Kwei San, Taoyuan, 333 Taiwan, R.O.C.

(Received October 24, 2002, Accepted September 16, 2003)

Abstract. A mixed eight-node hexahedral element formulated via the Hu-Washizu principle as well as the field extrapolation technique is presented. The mixed element with only three translational degrees of freedom at each node can provide extremely accurate and reliable performance for popular benchmark problems such as spacial beams, plates, shells as well as general three-dimensional elasticity problems. Numerical calculations also show that when extremely skewed and coarse meshes and nearly incompressible materials are used, the proposed mixed element can still possess excellent behaviour. The mixed formulation starts with introduction of a parallelepiped domain associated with the given general eight-node hexahedral element. Then, the assumed strain field at the nodal level is constructed via the Hu-Washizu variational principle for that associated parallelepiped domain. Finally, the assumed strain field at the nodal level of the given hexahedral element is established by using the field extrapolation technique, and then by using the trilinear shape functions the assumed strain field of the whole element domain is obtained. All matrices involved in establishing the element stiffness matrix can be evaluated analytically and expressed explicitly; however, a 24 by 24 matrix has to be inverted to construct the displacement extrapolation matrix. The proposed hexahedral element satisfies the patch test as long as the element with a shape of parallelepiped.

Key words: Hu-Washizu principle; field extrapolation; assumed strain formulation; eight-node parallelepiped; mixed formulation; shear and membrane locking.

1. Introduction

Existence of continuum finite element models with high predictive capabilities in both continuum and structural applications is very important in the analysis of various complex structural forms, that

[†] Section Chief

[‡] Assistant Professor

are common in civil, mechanical, and aerospace applications. These structural forms often include irregular geometry and cutouts, which form large two-dimensional or three-dimensional continuum zones connected by regions with dimensions characteristic of structural elements (e.g., beams, arches, plates, shells, etc.) rather than continuum. While the behaviour of continuum zones is governed by differential equations of the appropriate continuum, the connecting structure-like regions are more adequately described by higher order equations of structural mechanics. In situations like that, either a mixture of structural and continuum elements is needed or else a single continuum finite element model should be able to adequately represent the behaviour of large continuum zones and the behaviour of structural-like components of the system.

Existing commercial finite element codes usually include large libraries of continuum and structural finite elements. These finite element models often can be combined quite freely to form various structural forms. However, in many applications, the transition from the definitely structural-like zone to the clearly continuum zone is gradual and the user of a commercial package is forced to arbitrarily define the boundary between the two zones if two different finite element models are to be used. This is one example in which it has clearly advantageous to use one element model whose range of applicability covers both the continuum and structural parts. An additional aspect of this example testifying in favour of an appropriate single element is the sensitivity of the results on the type of the connection between the structural and continuum elements used in the code. This aspect would be totally bypassed if a single continuum element could be employed in the analysis.

Another example, where the continuum elements applicable to both continuum and structural problems are useful, can be found in the analysis of plates and shells. Here the so-called "degenerate continuum elements" have been used for a long time. The main reason behind that use is due to the fact that the continuum elements allowed to formulate shell (or plate) elements without intricacies of the shell theory. However it was immediately realized that the continuum finite element models were for shell too stiff - a phenomenon related to shear locking and membrane locking. In order to obtain meaningful solutions for shells, some 'modifications' of the continuum finite elements were necessary; but then the modified continuum finite elements for shells could not be used in the analysis of a general three-dimensional continuum. As the history of the shell analysis indicates, continuum elements need to be modified if their applicability is to be extended to structural problems. It is understandable that the need for the modification decreases as the order of the element sufficiently increases. High order elements are rich enough to incorporate a complex behaviour of any structural form. However, these elements are inefficient in the sense that their accuracy can be matched by the lower order, but properly developed continuum elements.

In recent years, researches in the development of efficient low order eight-node hexahedral elements (typically trilinear) have been extensively discussed in the literature. The main goal of the research is to improve its poor performance resulting from the presence of the so-called parasitic shear terms in the analysis of bending dominated situations. Such an inadequate performance of the eight-node hexahedral element is further deteriorated when highly distorted and high aspect ratio meshes are considered or when nearly incompressible materials are used. In addition, in the analysis of various geometrically complex structural forms in which a large number of elements may be needed to describe the geometric condition and to catch stress concentration phenomenon realistically. When low order elements with enhanced coarse mesh accuracy and improved bending properties are used in such a condition, a significant reduction in the computational efforts can also be achieved resulting from the reduction of global degrees of freedom. For nonlinear analysis, coarse and skewed mesh accuracy will become more important than that in the linear analysis. For

instance, under large deformation analysis, when a beam, originally modeled by regular 3D brick elements, is subjected to pure bending, cross section of the beam and the element's faces intersected by the vector in the bending direction will deform to a trapezoidal shape. This kind of deformed situation can be found quite common in the analysis, particularly, for bending dominated problems. As a result, it will be useful if an element can possess high accurate bending properties and extremely low sensitivity to mesh distortions.

Broadly speaking, representative methods emerged as a result of aiming at an improved bending properties of the low-order eight-node hexahedral element include: (1) Incompatible mode methods (Wilson *et al.* 1973, Taylor *et al.* 1976, Chandra and Prathap 1989, and others); (2) Drilling degrees of freedom methods (Yunus *et al.* 1991, Ibrahimbegovic and Wilson 1991, Sze *et al.* 1996, and others); (3) Mixed methods (Pian 1964, Pian and Chen 1983, Pian and Sumihara 1984, Pian and Tong 1986, Sze and Ghali 1993, Cheung and Chen 1988, Chen and Cheung 1992, Weissman 1996, Yeo and Lee 1997, Sze and Yao 2000, Cao *et al.* 2002, and others); (4) Reduced integration methods (Flanagan and Belytschko 1981, Wang and Belytschko 1987, and others); (5) Assumed strain methods (Belytschko and Bindeman, Chen and Stolarski 1998, and others). A more detailed and more extensive description of the above mentioned methods has been reported in Chen and Stolarski 1998, and the reader can refer there for details.

The basic idea proposed in Chen and Stolarski 1998 consists in introduction of a parallelepiped associated with a given general hexahedral element, subsequent formulations of the assumed strain field in this parallelepiped domain, and extrapolation of the displacement and assumed strain fields to the domain of the original hexahedral element. The eight-node assumed strain hexahedral elements proposed by Chen and Stolarski 1998 didn't pass the C^0 patch test for a general hexahedral shape. However, various numerical tests have confirmed their excellent convergence characteristics as long as the initially general form of the hexahedral element approaches a parallelepiped shape with the refinement of the mesh. In addition, they are also found to be very accurate and reliable for both structural and continuum mechanics problems while using coarse and irregular meshes in incompressible limits.

Very recently, a mixed four-node quadrilateral has been successfully formulated by means of the Hu-Washizu variation principle in conjunction with the concept of strain and displacement extrapolation (Chen 2002). Numerical performance demonstrates that the mixed element formulated in this way can provide excellent properties for both bending and membrane dominated problems. In this work, similar approach of using Hu-Washizu principle and field extrapolation technique is investigated to formulate a mixed eight-node hexahedral element. The assumed nodal strain of the associated parallelepiped is established via the Hu-Washizu principle and evaluated at the nodal level. Procedure of performing strain and displacement extrapolation (Chen and Stolarski 1998) is followed to establish the assumed strain field of the original hexahedral element. Predictions of the proposed mixed element for a variety of testing problems including element's response relating to the C^0 patch test are quite similar to those assumed strain elements provided in Chen and Stolarski 1998. However, the computational efforts required in formulating the element stiffness matrix of the element presented here have been greatly reduced.

The remainder of the paper is outlined as follows. General description of the Hu-Washizu principle and the procedure of establishing the assumed strain-displacement operator are given in Section 2. In Section 3, a parallelepiped domain associated with a given general eight-node hexahedral element is introduced. Finite element approximation based on the Hu-Washizu principle for the associated parallelepiped element is described in Section 4. In Section 5, concept of the

strain and displacement extrapolation are adopted to obtain the assumed strain field of the given hexahedral element. Section 6 describes test problems and numerical results obtained. The last section reports conclusions.

2. Hu-Washizu principle and assumed fields

For completeness, general procedure involved in deriving finite element model via Hu-Washizu principle as described by many researchers in the literatures is recalled hereinafter. The linearized Hu-Washizu variational principle states that all of the field equations and the natural boundary conditions can be obtained as the stationary conditions of the following linearized functional

$$\Pi_{HW}(\mathbf{u}, \boldsymbol{\sigma}, \boldsymbol{\varepsilon}^*) = \int_{\Omega} \left[\frac{1}{2} (\boldsymbol{\varepsilon}^*)^T \mathbf{D} \boldsymbol{\varepsilon}^* - \boldsymbol{\sigma}^T (\boldsymbol{\varepsilon}^* - \nabla_s \mathbf{u}) \right] d\Omega - \mathbf{P}, \quad (1)$$

where \mathbf{u} , $\boldsymbol{\sigma}$, and $\boldsymbol{\varepsilon}^*$ are the assumed displacement, stress, and strain fields, respectively; \mathbf{D} represents the matrix of material elastic constants; $\nabla_s \mathbf{u}$ is the symmetric part of the displacement gradient; Ω is the domain considered; \mathbf{P} states the potential of external work. In order to obtain the finite element formulations corresponding to the functional of Eq. (1), assumed fields \mathbf{u} , $\boldsymbol{\sigma}$, and $\boldsymbol{\varepsilon}^*$ have to be specified, and they are approximated over each element domain and expressed as follows

$$\mathbf{u} = \mathbf{N} \mathbf{d} \quad (\text{which leads to } \nabla_s \mathbf{u} = \mathbf{B} \mathbf{d}), \quad \boldsymbol{\sigma} = \mathbf{S} \mathbf{s}, \quad \boldsymbol{\varepsilon}^* = \mathbf{E} \mathbf{e}, \quad (2,3,4,5)$$

where \mathbf{d} , \mathbf{s} , and \mathbf{e} are the vectors of nodal displacements, independent stress parameters, and independent strain parameters, respectively; \mathbf{N} , \mathbf{S} , and \mathbf{E} are the shape functions for the displacements, stresses, and strains, respectively. Substituting the above assumed fields into the linearized Hu-Washizu functional and making this functional stationary with respect to \mathbf{d} , \mathbf{s} , and \mathbf{e} respectively, one gets

$$(1) \text{ Equilibrium equations: } \left[\int_{\Omega} \mathbf{B}^T \mathbf{S} \mathbf{d} \Omega \right] \mathbf{s} - \mathbf{f}^{\text{ext}} = 0, \quad (6)$$

$$(2) \text{ Strain-displacement relationships: } \left[\int_{\Omega} \mathbf{S}^T \mathbf{E} \mathbf{d} \Omega \right] \mathbf{e} - \left[\int_{\Omega} \mathbf{S}^T \mathbf{B} \mathbf{d} \Omega \right] \mathbf{d} = 0, \quad (7)$$

$$(3) \text{ Constitutive equations: } \left[\int_{\Omega} \mathbf{E}^T \mathbf{D} \mathbf{E} \mathbf{d} \Omega \right] \mathbf{e} - \left[\int_{\Omega} \mathbf{E}^T \mathbf{S} \mathbf{d} \Omega \right] \mathbf{s} = 0, \quad (8)$$

where \mathbf{f}^{ext} is the vector of external force resulting from body forces and natural boundary conditions. By using Eq. (5) and Eq. (7), the assumed strain field can be expressed in terms of the vector of element nodal displacements

$$\boldsymbol{\varepsilon}^* = \left\{ \mathbf{E} \left[\int_{\Omega} \mathbf{S}^T \mathbf{E} \mathbf{d} \Omega \right]^{-1} \left[\int_{\Omega} \mathbf{S}^T \mathbf{B} \mathbf{d} \Omega \right] \right\} \mathbf{d} = \mathbf{B}^* \mathbf{d}, \quad (9)$$

where \mathbf{B}^* is the assumed strain-displacement operator. Note that the assumed strain field of Eq. (9) can be obtained only when $\int_{\Omega} \mathbf{S}^T \mathbf{E} \mathbf{d} \Omega$ is invertible, and that in this work the domain considered under the framework of Hu-Washizu principle is referred to a parallelepiped, which is associated with a given general hexahedral element (to be explained in section 3).

3. The eight-node hexahedral element and its associated parallelepiped

For a general eight-node hexahedral element, an associated parallelepiped shown in Fig. 1 can always be defined. Its nodal position vectors $\mathbf{X}_{\hat{I}}$ of node \hat{I} is given by the following expressions

$$\mathbf{X}_{\hat{I}} = \mathbf{X}_{\hat{C}} + [\mathbf{G}_{\bar{\xi}} \mathbf{G}_{\bar{\eta}} \mathbf{G}_{\bar{\zeta}}] \{\hat{\xi}_{\hat{I}} \hat{\eta}_{\hat{I}} \hat{\zeta}_{\hat{I}}\}^T = X_{\hat{I}}^k \mathbf{e}_k, \quad \mathbf{X}_{\hat{C}} = \frac{1}{8} \sum_{I=1}^8 \mathbf{X}_I, \quad \mathbf{G}_{\bar{K}} = \frac{1}{8} \sum_{I=1}^8 K_I \mathbf{X}_I, \quad (10,11,12)$$

where $\mathbf{X}_{\hat{C}}$ is the position vector of point \hat{C} which is the centre of the associated parallelepiped, uppercase K represents parameters (ξ, η, ζ) , $\{\hat{\xi}_{\hat{I}} \hat{\eta}_{\hat{I}} \hat{\zeta}_{\hat{I}}\}^T$ is the vector of coordinates of the nodal point \hat{I} in the space of the isoparametric parameters $(\hat{\xi}, \hat{\eta}, \hat{\zeta})$ of the associated parallelepiped whereas $\{\xi_I, \eta_I, \zeta_I\}^T$ is the coordinates of the nodal point I in the space of isoparametric parameters (ξ, η, ζ) of the hexahedral element, \mathbf{X}_I is the nodal position vector at nodal point I of the hexahedral element, and subscript or superscript k represents k^{th} component of the vector relative to the fixed global system $\mathbf{e}_k = \mathbf{e}^k$. Throughout this work, indices repeated on two different levels imply summation over their range, the superscript “ T ” designates the transpose of a matrix, and a “ $\hat{}$ ” on the top indicates that a quantity is related to the associated parallelepiped, unless otherwise stated.

A physical natural coordinate system $(\bar{\xi}, \bar{\eta}, \bar{\zeta})$, as shown in Fig. 1, is defined and attached to point \hat{C} . Its definition is given as follows

$$\bar{K} = L_{\bar{K}} \hat{K}, \quad K = \xi, \eta, \zeta, \quad \text{which leads to} \quad \frac{\partial}{\partial \bar{K}} = \frac{1}{L_{\bar{K}}} \frac{\partial}{\partial \hat{K}}, \quad (14,15)$$

where $L_{\bar{K}}$ represents length of vector $\mathbf{G}_{\bar{K}}$ and a “ $\bar{}$ ” on the top indicates that a quantity is related to the $(\bar{\xi}, \bar{\eta}, \bar{\zeta})$ frame.

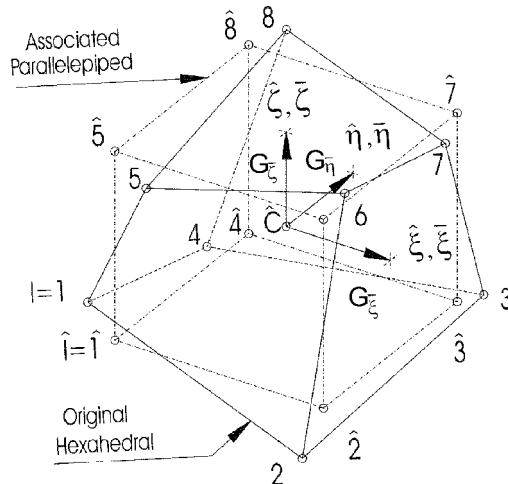


Fig. 1 The original Hexahedral and its associated parallelepiped

4. Finite element approximation for the associated parallelepiped element

In the context of Hu-Washizu variational principle, the finite element model is established by approximating three independent (assumed) fields. In this work, these three assumed fields are interpolated for the associated parallelepiped and expressed in the physical natural coordinates system. Construction and interpretation of these three assumed fields are, respectively, given in the following subsections.

4.1 Assumed covariant displacement field

From tensor algebra, the assumed covariant displacement field $\hat{\mathbf{u}}$ of the associated parallelepiped in the $(\bar{\xi}, \bar{\eta}, \bar{\zeta})$ frame can be related to that in the global fixed system and then, as usual, be approximated in terms of nodal displacements by using standard trilinear shape functions. The result is

$$\hat{\mathbf{u}}_{\bar{K}} = \left(\frac{\mathbf{G}_{\bar{K}}}{L_{\bar{K}}} \cdot \mathbf{e}^k \right) \hat{\mathbf{u}}_k = g_{\bar{K}}^k \hat{\mathbf{u}}_k = N^j g_{\bar{K}}^k \hat{\mathbf{u}}_{jk}, \quad N^j = \frac{1}{8} (1 + \hat{\xi}_i \hat{\xi}_i) (1 + \hat{\eta}_i \hat{\eta}_i) (1 + \hat{\zeta}_i \hat{\zeta}_i), \quad (16a,b)$$

where $\hat{\mathbf{u}}_{\bar{K}}$ is the \bar{K}^{th} component of $\hat{\mathbf{u}}$ in the $(\bar{\xi}, \bar{\eta}, \bar{\zeta})$ frame whereas $\hat{\mathbf{u}}_k$ represents the k^{th} component of $\hat{\mathbf{u}}$ relative to the global fixed system $\mathbf{e}_k = \mathbf{e}^k$, and N denotes the standard trilinear shape functions. By virtue of the assumed covariant displacement field defined above, the corresponding covariant strain field $\hat{\bar{\boldsymbol{\varepsilon}}}$ of the associated parallelepiped in the $(\bar{\xi}, \bar{\eta}, \bar{\zeta})$ frame can be evaluated by using the following well-known linear strain-displacement equations

$$\hat{\bar{\boldsymbol{\varepsilon}}}_{\bar{K}\bar{L}} = \frac{1}{2} (\hat{\mathbf{u}}_{\bar{K},\bar{L}} + \hat{\mathbf{u}}_{\bar{L},\bar{K}}), \quad (17)$$

which leads to the covariant strain field of the associated parallelepiped as follows

$$\bar{\boldsymbol{\varepsilon}} = \{ \hat{\bar{\boldsymbol{\varepsilon}}}_{\bar{\xi}\bar{\xi}} \quad \hat{\bar{\boldsymbol{\varepsilon}}}_{\bar{\eta}\bar{\eta}} \quad \hat{\bar{\boldsymbol{\varepsilon}}}_{\bar{\zeta}\bar{\zeta}} \quad 2\hat{\bar{\boldsymbol{\varepsilon}}}_{\bar{\xi}\bar{\eta}} \quad 2\hat{\bar{\boldsymbol{\varepsilon}}}_{\bar{\eta}\bar{\zeta}} \quad 2\hat{\bar{\boldsymbol{\varepsilon}}}_{\bar{\xi}\bar{\zeta}} \}^T = \bar{\mathbf{B}} \hat{\mathbf{d}}, \quad (18a)$$

$$\bar{\mathbf{B}}_i^k = \left\{ \frac{g_{\bar{\xi}}^k N_{,\bar{\xi}}^j}{L_{\bar{\xi}}} \frac{g_{\bar{\eta}}^k N_{,\bar{\eta}}^j}{L_{\bar{\eta}}} \frac{g_{\bar{\zeta}}^k N_{,\bar{\zeta}}^j}{L_{\bar{\zeta}}} \frac{g_{\bar{\xi}}^k N_{,\bar{\eta}}^j}{L_{\bar{\eta}}} + \frac{g_{\bar{\eta}}^k N_{,\bar{\xi}}^j}{L_{\bar{\xi}}} \frac{g_{\bar{\eta}}^k N_{,\bar{\zeta}}^j}{L_{\bar{\zeta}}} + \frac{g_{\bar{\zeta}}^k N_{,\bar{\xi}}^j}{L_{\bar{\xi}}} \frac{g_{\bar{\zeta}}^k N_{,\bar{\eta}}^j}{L_{\bar{\eta}}} + \frac{g_{\bar{\zeta}}^k N_{,\bar{\xi}}^j}{L_{\bar{\xi}}} \right\}^T, \quad (18b)$$

where $N_{,\bar{K}}^j$ denotes $\partial N^j / \partial \bar{K}$, and $\hat{\mathbf{d}}$ is the vector of element nodal displacements of the associated parallelepiped. From tensor algebra, the conventional covariant strain field $\hat{\boldsymbol{\varepsilon}}$ in the global fixed frame can be related to $\hat{\bar{\boldsymbol{\varepsilon}}}$ of Eq. (18a) as follows

$$\hat{\boldsymbol{\varepsilon}}_{ij} = g_i^{\bar{K}} g_j^{\bar{L}} \hat{\bar{\boldsymbol{\varepsilon}}}_{\bar{K}\bar{L}}, \quad \text{or in the matrix form } \hat{\boldsymbol{\varepsilon}} = \boldsymbol{\Gamma}_\varepsilon \bar{\boldsymbol{\varepsilon}}, \quad (19)$$

4.2 Assumed contravariant stress field

In the development of finite element models, suppression of any possible zero-energy deformation modes is necessary for satisfying stability considerations in the analysis. Pian and Chen 1983 proposed a systematic approach in determining the necessary assumed stress parameters for

assumed stress hybrid models such that zero-energy deformation modes can be eliminated on element level. As suggested by Pian and Chen 1983, the optimal number of stress parameters is equal to the total number of displacement degrees of freedom minus the number of rigid body modes, but with the suppression of the zero-energy deformation modes. Many research results have also indicated that assumed stress hybrid elements will behave too stiff if stress parameters are overused. For an 8-node hexahedral element, the optimal number of stress modes will be $3 \times 8 - 6 = 18$. Pian and Tong 1986 established 18 β -stress parameters in the formulation of 8-node hexahedral hybrid element. These 18 β -stress terms are exactly the same as that discussed in Pian and Chen 1983. Following the same shape functions proposed by Pian and Tong 1986, the assumed contravariant stress field of the associated parallelepiped in the coordinates system $(\bar{\xi}, \bar{\eta}, \bar{\zeta})$ is approximated by

$$\bar{\boldsymbol{\sigma}} = \{\hat{\boldsymbol{\sigma}}^{\bar{\xi}\bar{\xi}} \hat{\boldsymbol{\sigma}}^{\bar{\eta}\bar{\eta}} \hat{\boldsymbol{\sigma}}^{\bar{\zeta}\bar{\zeta}} \hat{\boldsymbol{\sigma}}^{\bar{\xi}\bar{\eta}} \hat{\boldsymbol{\sigma}}^{\bar{\eta}\bar{\zeta}} \hat{\boldsymbol{\sigma}}^{\bar{\xi}\bar{\zeta}}\}^T = \begin{bmatrix} \hat{\mathbf{S}}^{cb} & \mathbf{0} \\ \mathbf{0} & \hat{\mathbf{S}}^s \end{bmatrix} \begin{Bmatrix} \hat{\mathbf{s}}^{cb} \\ \hat{\mathbf{s}}^s \end{Bmatrix} = \hat{\mathbf{S}}\hat{\mathbf{s}}, \quad (20a)$$

$$\hat{\mathbf{S}}^{cb} = \begin{Bmatrix} 1 & \hat{\eta} & \hat{\zeta} & \hat{\eta}\hat{\zeta} & 0 & 0 & 0 & 0 & 0 & 0 & 0 & 0 \\ 0 & 0 & 0 & 0 & 1 & \hat{\xi} & \hat{\zeta} & \hat{\xi}\hat{\zeta} & 0 & 0 & 0 & 0 \\ 0 & 0 & 0 & 0 & 0 & 0 & 0 & 0 & 1 & \hat{\xi} & \hat{\eta} & \hat{\xi}\hat{\eta} \end{Bmatrix}, \quad \hat{\mathbf{S}}^s = \begin{Bmatrix} 1 & \hat{\zeta} & 0 & 0 & 0 & 0 \\ 0 & 0 & 1 & \hat{\xi} & 0 & 0 \\ 0 & 0 & 0 & 0 & 1 & \hat{\eta} \end{Bmatrix}, \quad (20b,c)$$

where the uppercase $\hat{\mathbf{S}}$ is the matrix of shape functions describing the distribution of the assumed contravariant stresses in the associated parallelepiped while the lowercase $\hat{\mathbf{s}}$ is the vector comprised of eighteen independent stress parameters; the superscript “ cb ” indicates that quantities will match with three constant strain modes $(\hat{\boldsymbol{\varepsilon}}_{xx}^C, \hat{\boldsymbol{\varepsilon}}_{yy}^C, \hat{\boldsymbol{\varepsilon}}_{zz}^C)$, six constant bending modes, and three linear bending modes as defined in Eqs. (32, 37, 40); and the superscript “ s ” denotes that quantities will match with three constant shear strain modes $(2\hat{\boldsymbol{\varepsilon}}_{xy}^C, 2\hat{\boldsymbol{\varepsilon}}_{yz}^C, 2\hat{\boldsymbol{\varepsilon}}_{xz}^C)$ and three linear shear modes as described in Eqs. (32, 34). For the associated parallelepiped, the contravariant stress $\bar{\boldsymbol{\sigma}}$ is expressed in terms of stress parameters $\hat{\mathbf{s}}$, which is independent from one element to the other. And each stress parameter matches individually with one deformation mode specified in Eq. (30) excluding six rigid body modes. For an associated parallelepiped, stresses induced by those deformation modes are relatively clear and consistent with the variation of $\bar{\boldsymbol{\sigma}}$. For instance, $\hat{\boldsymbol{\sigma}}^{\bar{\xi}\bar{\xi}}$ is expressed by shape functions $[1, \hat{\eta}, \hat{\zeta}, \hat{\eta}\hat{\zeta}]$ and the first four stress parameters of the vector $\hat{\mathbf{s}}^{cb}$. Each term of shape functions $[1, \hat{\eta}, \hat{\zeta}, \hat{\eta}\hat{\zeta}]$ matches, respectively, with the stress induced from constant strain mode $\hat{\boldsymbol{\varepsilon}}_{xx}^C$, constant bending modes $\hat{\beta}_{\bar{\eta}}$ and $\hat{\beta}_{\bar{\zeta}}$, and linear bending mode $\hat{\theta}_{\bar{\xi}}$ as stated in Eqs. (32, 37, 40). Similar explanation can be given for other stress components. Similarly, by virtue of tensor algebra, the conventional contravariant stress field $\hat{\boldsymbol{\sigma}}$ of the associated parallelepiped in the global fixed frame can be related to $\bar{\boldsymbol{\sigma}}$ of Eq. (20a) as follows

$$\hat{\boldsymbol{\sigma}}_{ij} = g_{\bar{k}i}g_{\bar{l}j}\hat{\boldsymbol{\sigma}}^{\bar{k}\bar{l}}, \quad \text{or in the matrix form} \quad \hat{\boldsymbol{\sigma}} = \boldsymbol{\Gamma}_{\sigma}\bar{\boldsymbol{\sigma}} = \boldsymbol{\Gamma}_e\bar{\boldsymbol{\sigma}}. \quad (21)$$

4.3 Assumed covariant strain field

Adopting the same shape functions of Eqs. (20b,c) and incorporating some modifications to take the effects of Poisson’s ratio into account, the assumed (modified) covariant strain field of the

associated parallelepiped in the $(\bar{\xi}, \bar{\eta}, \bar{\zeta})$ frame is approximated by

$$\bar{\mathbf{e}}^* = \{\hat{\mathbf{e}}_{\bar{\xi}\bar{\xi}}^* \hat{\mathbf{e}}_{\bar{\eta}\bar{\eta}}^* \hat{\mathbf{e}}_{\bar{\zeta}\bar{\zeta}}^* 2\hat{\mathbf{e}}_{\bar{\xi}\bar{\eta}}^* 2\hat{\mathbf{e}}_{\bar{\eta}\bar{\zeta}}^* 2\hat{\mathbf{e}}_{\bar{\xi}\bar{\zeta}}^*\}^T = \begin{bmatrix} \hat{\mathbf{E}}^{cb} & \mathbf{0} \\ \mathbf{0} & \hat{\mathbf{S}}^s \end{bmatrix} \begin{Bmatrix} \hat{\mathbf{e}}^{cb} \\ \hat{\mathbf{e}}^s \end{Bmatrix} = \hat{\mathbf{E}}\hat{\mathbf{e}}, \quad (22a)$$

$$\hat{\mathbf{E}}^{cb} = \begin{bmatrix} 1 & \hat{\eta} & \hat{\zeta} & \hat{\eta}\hat{\zeta} & 0 & -\hat{v}\hat{\xi} & 0 & -\hat{v}\hat{\xi}\hat{\zeta} & 0 & -\hat{v}\hat{\xi} & 0 & -\hat{v}\hat{\xi}\hat{\eta} \\ 0 & -\hat{v}\hat{\eta} & 0 & -\hat{v}\hat{\eta}\hat{\zeta} & 1 & \hat{\xi} & \hat{\zeta} & \hat{\xi}\hat{\zeta} & 0 & 0 & -\hat{v}\hat{\eta} & -\hat{v}\hat{\xi}\hat{\eta} \\ 0 & 0 & -\hat{v}\hat{\zeta} & -\hat{v}\hat{\eta}\hat{\zeta} & 0 & 0 & -\hat{v}\hat{\zeta} & -\hat{v}\hat{\xi}\hat{\zeta} & 1 & \hat{\xi} & \hat{\eta} & \hat{\xi}\hat{\eta} \end{bmatrix}, \quad (22b)$$

where $\hat{\mathbf{E}}$ is the matrix of shape functions used to describe the assumed covariant strain field in the associated parallelepiped, $\hat{\mathbf{e}}$ is the vector comprised of eighteen independent strain parameters, $\hat{v} = v/(1-v)$, and v is the Poisson's ratio. In the above equation, \hat{v} and v are used to take into account the effects of Poisson's ratio for the assumed covariant strain field corresponding to the bending part. Since that shape functions $\hat{\mathbf{E}}$ are used to express the variation of $\bar{\mathbf{e}}^*$, incorporation of Poisson's ratio in $\hat{\mathbf{E}}$ provides modification of strain field such that each strain parameter matches individually with one deformation mode specified in Eq. (30). For instance, constant bending mode $\hat{\gamma}_{\bar{\zeta}}$ in Eq. (37) represents the rigid body rotation of the pyramid $\hat{C}\hat{2}\hat{3}\hat{7}\hat{6}$ about the vector $\mathbf{G}_{\bar{\zeta}}$ while keeping pyramid $\hat{C}\hat{1}\hat{4}\hat{8}\hat{5}$ fixed. It describes the mode of deformation in which stretching of the parametric lines (in $\mathbf{G}_{\bar{\xi}}$ direction) varies linearly in the direction of $\mathbf{G}_{\bar{\eta}}$. This deformed configuration creates a strain state matches with the variation of strain $\hat{\mathbf{e}}_{\bar{\xi}\bar{\xi}}^*$, the part expressed by the shape function $[\hat{\eta}]$ and the second strain parameter of the vector $\hat{\mathbf{e}}^{cb}$. If Poisson's ratio is not equal to zero, it will generate stretching of the parametric lines in $\mathbf{G}_{\bar{\zeta}}$ direction varies linearly in the direction of $\mathbf{G}_{\bar{\eta}}$. This is a deformed situation similar to that generated by bending mode $\hat{\gamma}_{\bar{\xi}}$ (in negative direction). This Poisson's ratio related strain matches with the variation of strain $\hat{\mathbf{e}}_{\bar{\eta}\bar{\eta}}^*$, the part expressed by the shape function $[-\hat{v}\hat{\eta}]$ and the second strain parameter of the vector $\hat{\mathbf{e}}^{cb}$. It provides justification of introducing Poisson's ratio in 2nd column of matrix $\hat{\mathbf{E}}^{cb}$. Similar explanation can be given for other strain components. Note that no modification of constant strain and linear shear strain is needed.

With the use of shape functions $\hat{\mathbf{S}}$ of Eq. (20a) and $\hat{\mathbf{E}}$ of Eq. (22a), and since that the determinant of the Jacobian is constant for any parallelepiped, integration of $\hat{\mathbf{S}}^T\hat{\mathbf{E}}$ over the associated parallelepiped domain can be easily achieved as follows

$$\int_{\hat{\Omega}} \hat{\mathbf{S}}^T \hat{\mathbf{E}} d\hat{\Omega} = 8|\hat{\mathbf{J}}| \left[\text{diag} \left\{ 1 \frac{1}{3} \frac{1}{3} \frac{1}{9} 1 \frac{1}{3} \frac{1}{3} \frac{1}{9} 1 \frac{1}{3} \frac{1}{3} \frac{1}{9} 1 \frac{1}{3} 1 \frac{1}{3} 1 \frac{1}{3} \right\} \right] \quad (23)$$

where $|\hat{\mathbf{J}}|$ represents one eighth of the volume of the associated parallelepiped. Since that Eq. (23) is a diagonal matrix, inverse of Eq. (23) can be easily obtained. The result is

$$\left[\int_{\hat{\Omega}} \hat{\mathbf{S}}^T \hat{\mathbf{E}} d\hat{\Omega} \right]^{-1} = \frac{1}{8|\hat{\mathbf{J}}|} [\text{diag}\{1 \ 3 \ 3 \ 9 \ 1 \ 3 \ 3 \ 9 \ 1 \ 3 \ 3 \ 9 \ 1 \ 3 \ 1 \ 3 \ 1 \ 3\}]. \quad (24)$$

By using the matrix $\hat{\mathbf{S}}$ of Eq. (20a) and matrix $\bar{\mathbf{B}}_i^k$ of Eq. (18b), explicit expression of $\int_{\hat{\Omega}} \hat{\mathbf{S}}^T \bar{\mathbf{B}}_i^k d\hat{\Omega}$ can also be evaluated analytically as follows

$$\int_{\hat{\Omega}} \hat{\mathbf{S}}^T \bar{\mathbf{B}}_i^k d\hat{\Omega} = |\hat{\mathbf{J}}| \{ \phi_{\xi}^{\xi} \mathbf{\Lambda}_1^T \quad \phi_{\eta}^{\eta} \mathbf{\Lambda}_2^T \quad \phi_{\zeta}^{\zeta} \mathbf{\Lambda}_3^T \quad \mathbf{\Lambda}_4^T \}^T, \quad (25a)$$

$$\mathbf{\Lambda}_1^T = \{1 \quad \lambda_{\eta} \quad \lambda_{\zeta} \quad \lambda_{\eta} \quad \lambda_{\zeta}\}, \quad \mathbf{\Lambda}_2^T = \{1 \quad \lambda_{\xi} \quad \lambda_{\zeta} \quad \lambda_{\xi} \quad \lambda_{\zeta}\}, \quad \mathbf{\Lambda}_3^T = \{1 \quad \lambda_{\xi} \quad \lambda_{\eta} \quad \lambda_{\xi} \quad \lambda_{\eta}\}, \quad (25b,c,d)$$

$$\mathbf{\Lambda}_4^T = \{ \phi_{\eta}^{\xi} + \phi_{\xi}^{\eta} \quad \lambda_{\zeta}(\phi_{\eta}^{\xi} + \phi_{\xi}^{\eta}) \quad \phi_{\zeta}^{\eta} + \phi_{\eta}^{\zeta} \quad \lambda_{\xi}(\phi_{\zeta}^{\eta} + \phi_{\eta}^{\zeta}) \quad \phi_{\zeta}^{\xi} + \phi_{\xi}^{\zeta} \quad \lambda_{\eta}(\phi_{\zeta}^{\xi} + \phi_{\xi}^{\zeta}) \}, \quad (25e)$$

$$\phi_{\#}^* = \frac{\hat{\#}_I}{L_{\#}} g_{\#}^k, \quad \lambda_{\#} = \frac{L_{\#} \hat{\#}_I}{3}, \quad \#, * = \xi, \eta, \zeta. \quad (25f)$$

Noting that Eq. (23) and Eq. (25a) are evaluated in the natural coordinate system; however, the results given in Eq. (23) and Eq. (25a) are also valid in the fixed global system since that $\mathbf{\Gamma}_{\sigma}^T \mathbf{\Gamma}_{\varepsilon} = \mathbf{I}$ (unit matrix) holds for both regular and irregular elements. Substitution of matrix $\hat{\mathbf{E}}$ of Eq. (22a), Eq. (24), and Eq. (25a) into Eq. (9), the explicit form of assumed covariant strain field $\bar{\hat{\boldsymbol{\varepsilon}}}$ for the associated parallelepiped can then be expressed in terms of $\hat{\mathbf{d}}$ as follows

$$\bar{\hat{\boldsymbol{\varepsilon}}}^* = \left\{ \hat{\mathbf{E}} [\int_{\hat{\Omega}} \hat{\mathbf{S}}^T \hat{\mathbf{E}} d\hat{\Omega}]^{-1} [\int_{\hat{\Omega}} \hat{\mathbf{S}}^T \bar{\mathbf{B}} d\hat{\Omega}] \right\} \hat{\mathbf{d}} = \bar{\mathbf{B}}^* \hat{\mathbf{d}}. \quad (26)$$

In order to obtain the extrapolated nodal values of the assumed strain field for the original hexahedral element, nodal values of the assumed strain field with respect to the associated parallelepiped need to be evaluated. It can be easily accomplished by substituting the isoparametric coordinates of each nodal point $\hat{\mathbf{J}}$ into Eq. (26a). The result is

$$\bar{\hat{\boldsymbol{\varepsilon}}}_j^* = \bar{\mathbf{B}}^* (\hat{\xi} = \hat{\xi}_j, \hat{\eta} = \hat{\eta}_j, \hat{\zeta} = \hat{\zeta}_j) \hat{\mathbf{d}} = \bar{\mathbf{B}}_j^* \hat{\mathbf{d}}. \quad (27)$$

5. Assumed strain field for the eight-node hexahedral element

The assumed strain field $\bar{\hat{\boldsymbol{\varepsilon}}}_j^*$ of Eq. (27) is evaluated at the nodal points of the associated parallelepiped and expressed in terms of its nodal displacements. Therefore, in order to obtain the assumed strain field for the original hexahedral element, strain and displacement extrapolations identical to that proposed by Chen and Stolarski 1998 are implemented. It leads to the assumed strain-displacement operator for the original hexahedral element. For completeness, the procedure required to achieve this goal is outlined hereinafter.

5.1 Strain extrapolation

The extrapolation of the strain field at the nodal level is implemented by using the trilinear shape functions. The result is given by the following expressions

$$\bar{\hat{\boldsymbol{\varepsilon}}}_I^* = \mathbf{N}_I^j \bar{\hat{\boldsymbol{\varepsilon}}}_j^* = \bar{\mathbf{B}}_I^* \hat{\mathbf{d}}, \quad \mathbf{N}_I^j = \frac{1}{8} (1 + \hat{\xi}_j \hat{\xi}_I) (1 + \hat{\eta}_j \hat{\eta}_I) (1 + \hat{\zeta}_j \hat{\zeta}_I), \quad (28a,b)$$

where $\bar{\hat{\boldsymbol{\varepsilon}}}_I^*$ is the extrapolated nodal values of the assumed strain field for the original hexahedral element and $\{\hat{\xi}_I, \hat{\eta}_I, \hat{\zeta}_I\}$ are the coordinates of the nodal point I in the space of isoparametric parameters $\{\hat{\xi}, \hat{\eta}, \hat{\zeta}\}$ given by

$$\{\hat{\xi}_I, \hat{\eta}_I, \hat{\zeta}_I\}^T = [\mathbf{G}_{\xi} \quad \mathbf{G}_{\eta} \quad \mathbf{G}_{\zeta}]^{-1} \{\mathbf{X}_I - \mathbf{X}_C\}. \quad (28c)$$

5.2 Displacement extrapolation

As shown in Eq. (28a), $\bar{\boldsymbol{\epsilon}}_i^*$ is still expressed in terms of the nodal displacement of the associated parallelepiped. To relate the vector of element nodal displacements of the associated parallelepiped to that of the original hexahedral element, the following expression need to be established

$$\hat{\boldsymbol{d}} = \boldsymbol{\Psi} \boldsymbol{d}, \quad (29)$$

where $\boldsymbol{\Psi}$ denotes the displacement extrapolation matrix (to be defined in section 5.2.2), and \boldsymbol{d} represents the vector of element nodal displacements of the original hexahedral element.

The procedure of establishing the displacement extrapolation matrix starts with the identification of deformation modes for the original hexahedral element and its associated parallelepiped. With the deformation modes participating in the deformation process identified, the vector of element nodal displacements of the original hexahedral element and that of the associated parallelepiped can be expressed in terms of those modes of deformation. Eventually, by postulating that those deformation modes are common for both original hexahedral element and the associated parallelepiped, Eq. (29) can be obtained. Since that extrapolation of displacement field is much more intricate, for more detailed discussion readers can refer to Chen and Stolarski 1998. In this work, general procedure and presentation will be provided for completeness.

5.2.1 Identification of deformation modes

For a general eight-node hexahedral element, there are totally twenty-four modes of deformation corresponding to twenty-four degrees of freedom. They consist of twelve constant strain modes (six rigid body motion modes and six constant strain modes), three linear shear (warping) modes, six constant bending modes, and three linear bending modes. Deformed configurations for a cubic shape of hexahedral element of the linear shear modes, constant bending modes, and linear bending modes are depicted in Chen and Stolarski 1998. By virtue of the mode decomposition technique in conjunction with the identification of deformation modes mentioned above, the vector of the element nodal displacements can be decomposed and expressed in terms of those modes of deformation for the associated parallelepiped and the original hexahedral element, respectively, as follows

$$\hat{\boldsymbol{d}} = \hat{\boldsymbol{d}}^C + \hat{\boldsymbol{d}}^{LS} + \hat{\boldsymbol{d}}^{CB} + \hat{\boldsymbol{d}}^{LB} = \hat{\boldsymbol{C}}\hat{\boldsymbol{P}}^C + \hat{\boldsymbol{H}}^{LS}\hat{\boldsymbol{P}}^{LS} + \hat{\boldsymbol{H}}^{CB}\hat{\boldsymbol{P}}^{CB} + \hat{\boldsymbol{H}}^{LB}\hat{\boldsymbol{P}}^{LB} = \hat{\boldsymbol{H}}\hat{\boldsymbol{P}}, \quad (30)$$

$$\boldsymbol{d} = \boldsymbol{d}^C + \boldsymbol{d}^{LS} + \boldsymbol{d}^{CB} + \boldsymbol{d}^{LB} = \boldsymbol{C}\boldsymbol{P}^C + \boldsymbol{H}^{LS}\boldsymbol{P}^{LS} + \boldsymbol{H}^{CB}\boldsymbol{P}^{CB} + \boldsymbol{H}^{LB}\boldsymbol{P}^{LB} = \boldsymbol{H}\boldsymbol{P}, \quad (31)$$

where superscripts “C”, “LS”, “CB”, and “LB” indicate that quantities are related to constant strain modes $\hat{\boldsymbol{P}}^C$ (or \boldsymbol{P}^C), linear shear modes $\hat{\boldsymbol{P}}^{LS}$ (or \boldsymbol{P}^{LS}), constant bending modes $\hat{\boldsymbol{P}}^{CB}$ (or \boldsymbol{P}^{CB}), and linear bending modes $\hat{\boldsymbol{P}}^{LB}$ (or \boldsymbol{P}^{LB}), respectively. The twenty-four deformation modes participating in the deformation process will be briefly described and be specified quantitatively for both the associated parallelepiped and the original hexahedral element in the subsequent formulation.

5.2.1.1 Constant strain modes

The rigid body and constant strain modes of the associated parallelepiped are represented by the following set of parameters

$$\hat{\mathbf{P}}^C = \{\hat{u}_1^1 \ \hat{u}_1^2 \ \hat{u}_1^3 \ \hat{\phi}_1^1 \ \hat{\phi}_1^2 \ \hat{\phi}_1^3 \ \hat{\boldsymbol{\varepsilon}}_{xx}^C \ \hat{\boldsymbol{\varepsilon}}_{yy}^C \ \hat{\boldsymbol{\varepsilon}}_{zz}^C \ 2\hat{\boldsymbol{\varepsilon}}_{xy}^C \ 2\hat{\boldsymbol{\varepsilon}}_{yz}^C \ 2\hat{\boldsymbol{\varepsilon}}_{xz}^C\}^T, \quad (32)$$

where \hat{u}_1^i is translational displacement of node $\hat{1}$ in global e^i -direction, $\hat{\phi}_1^i$ is the rigid body rotation of the element about global e^i -direction at node $\hat{1}$, and $\hat{\boldsymbol{\varepsilon}}_{ij}^C$ represent a constant part of the strain field.

The above definition of constant strain modes leads to the following equations representing the matrix $\hat{\mathbf{C}}$ of Eq. (30). Matrix $\hat{\mathbf{C}}$ is a 24×12 matrix containing constants dependent on the nodal coordinates and is partitioned into eight 3×12 matrices corresponding to eight nodal points of the associated parallelepiped as follows

$$\hat{\mathbf{C}} = [\hat{\mathbf{C}}_1^T \ \hat{\mathbf{C}}_2^T, \dots, \hat{\mathbf{C}}_7^T, \dots, \hat{\mathbf{C}}_8^T]^T, \quad (33a)$$

$$\hat{\mathbf{C}}_i = [\mathbf{I}_{3 \times 3} \ A_{i1k} e^k \ A_{i2k} e^k \ A_{i3k} e^k \ B_{i1}^1 e^1 \ B_{i1}^2 e^2 \ B_{i1}^3 e^3 \ B_{i2}^1 e^1 \ B_{i2}^2 e^2 \ B_{i2}^3 e^3], \quad (33b)$$

$$A_{i\hat{j}an} = (X_i^k - X_j^k) e_{akn}, \quad B_{i\hat{j}}^k = (X_i^k - X_j^k), \quad (33c,d)$$

where $\mathbf{I}_{3 \times 3}$ is a 3×3 unit matrix, and the symbol e_{akn} stands for the component of the permutation tensor. Based on the same postulation, vector \mathbf{P}^C and matrix \mathbf{C} of Eq. (31) can be established for the original hexahedral element. They are constructed in exactly the same way as for the associated parallelepiped.

5.2.1.2 Linear shear modes

The linear shear modes for the associated parallelepiped are represented by the following parameters

$$\hat{\mathbf{P}}^{LS} = \{S_{\bar{\xi}} \ S_{\bar{\eta}} \ S_{\bar{\zeta}}\}^T. \quad (34)$$

In the above equation, the subscripts indicate that the deformation mode they are related to will cause no shear deformation on the pair of faces which will be intersected by the vector \mathbf{G} with the same subscript. For instance, the linear shear (warping) mode $S_{\bar{\xi}}$ is designed in such a way that faces $\hat{1}\hat{4}\hat{8}\hat{5}$ and $\hat{2}\hat{3}\hat{7}\hat{6}$ (see Fig. 1), which will be intersected by vector $\mathbf{G}_{\bar{\xi}}$, deform with no change in length along the edges and diagonals of those two faces. Thus, the nodal displacement vectors have to be perpendicular to those faces. However, the remaining four faces will undergo shear deformation, their diagonals will change in length while the length of the edges will remain unchanged. The modes $S_{\bar{\eta}}$ and $S_{\bar{\zeta}}$ are defined similarly.

According to the deformed configuration described above, the relationship between vectors $\hat{\mathbf{d}}^{LS}$ and $\hat{\mathbf{P}}^{LS}$ can then be constructed. Matrix $\hat{\mathbf{H}}^{LS}$ in Eq. (30) is composed of eight 3×3 matrices. Those 3×3 matrices for node \hat{I} of the associated parallelepiped are given by the following expressions

$$\hat{\mathbf{H}}_I^{LS} = [\hat{\eta}_I \hat{\zeta}_I \mathbf{g}^{\bar{\xi}} \ \hat{\zeta}_I \hat{\xi}_I \mathbf{g}^{\bar{\eta}} \ \hat{\xi}_I \hat{\eta}_I \mathbf{g}^{\bar{\zeta}}], \quad g_{\bar{k}} \cdot g^{\bar{l}} = \delta_{\bar{k}}^{\bar{l}}, \quad (35a,b)$$

where $\delta_{\bar{k}}^{\bar{l}}$ stands for the Kronecker delta. To preserve those linear shear properties for the original hexahedral element, the part of matrix \mathbf{H}^{LS} of Eq. (31) related to node I of the original hexahedral element is extrapolated from the matrix $\hat{\mathbf{H}}_I^{LS}$ of Eq. (35a) by using the trilinear shape functions. The result is

$$\mathbf{H}_I^{LS} = N_I^{\hat{j}} \hat{\mathbf{H}}_j^{LS} \quad (36)$$

where $N_I^{\hat{j}}$ is identified in Eq. (28b). As a result of that extrapolation, the length along all edges of the original hexahedral element is no longer necessarily remaining unchanged.

5.2.1.3 Constant bending modes

For the deformation modes related to the constant bending strain field of the associated parallelepiped, the following set of parameters is used

$$\hat{\mathbf{P}}^{CB} = \{ \{ \hat{\alpha}_{\bar{\xi}} \ \hat{\alpha}_{\bar{\eta}} \} \{ \hat{\beta}_{\bar{\eta}} \ \hat{\beta}_{\bar{\zeta}} \} \{ \hat{\gamma}_{\bar{\zeta}} \ \hat{\gamma}_{\bar{\xi}} \} \}^T, \quad (37)$$

where subscripts $\bar{\xi}$, $\bar{\eta}$ and $\bar{\zeta}$ denote, respectively, the axes of rotation with the positive direction defined by vectors $\mathbf{G}_{\bar{\xi}}$, $\mathbf{G}_{\bar{\eta}}$, and $\mathbf{G}_{\bar{\zeta}}$. It is noted that the parameters listed above and named using the same letter ($\hat{\alpha}$, $\hat{\beta}$, or $\hat{\gamma}$) are considered to be a pair which will participate in the deformation process simultaneously. The constant bending mode $\hat{\alpha}_{\bar{\xi}}$, for instance, represents the rigid body rotation of the pyramid $\hat{C}\hat{4}\hat{3}\hat{7}\hat{8}$ about the vector $\mathbf{G}_{\bar{\xi}}$ while keeping pyramid $\hat{C}\hat{1}\hat{2}\hat{6}\hat{5}$ fixed. It describes the mode of deformation in which stretching of the parametric lines (in $\mathbf{G}_{\bar{\eta}}$ direction) varies linearly in the direction of $\mathbf{G}_{\bar{\zeta}}$. This is reminiscent of the strain distribution in beam under pure bending, even though no curvature of the parametric lines is present. And if Poisson's ratio is not equal to zero, bending mode $\hat{\alpha}_{\bar{\xi}}$ will also generate stretching of the parametric lines in $\mathbf{G}_{\bar{\xi}}$ direction varies linearly in the direction of $\mathbf{G}_{\bar{\zeta}}$. This is a deformed situation similar to that generated by bending mode $\hat{\alpha}_{\bar{\eta}}$ (in negative direction). It provides justification of introducing Poisson's ratio in the matrix $\hat{\mathbf{E}}^{cb}$, 7th and 3th columns, of Eq. (22b) for constant bending modes $\hat{\alpha}_{\bar{\xi}}$ and $\hat{\alpha}_{\bar{\eta}}$, respectively. Similar explanation can be given for the other two pairs of constant bending modes. Presence of the constant bending modes is crucial for an element to be applicable in most structural situations. Based on the deformed pattern specified above, matrix $\hat{\mathbf{H}}^{CB}$ in Eq. (30) can be obtained. It is composed of eight 3×6 matrices, and its eight parts corresponding to nodes \hat{I} are given as follows

$$\hat{\mathbf{H}}_I^{CB} = (X_I^k - X_C^k) e_{mkn} e^n [G_{\bar{\xi}}^m \delta_I^{\hat{O}} \ G_{\bar{\eta}}^m \delta_I^{\hat{P}} \ G_{\bar{\eta}}^m \delta_I^{\hat{Q}} \ G_{\bar{\zeta}}^m \delta_I^{\hat{R}} \ G_{\bar{\zeta}}^m \delta_I^{\hat{S}} \ G_{\bar{\xi}}^m \delta_I^{\hat{T}}], \quad (38)$$

where variables O , P , Q , R , S , and T , which are, respectively, used corresponding to constant bending modes $\hat{\alpha}_{\bar{\xi}}$, $\hat{\alpha}_{\bar{\eta}}$, $\hat{\beta}_{\bar{\eta}}$, $\hat{\beta}_{\bar{\zeta}}$, $\hat{\gamma}_{\bar{\zeta}}$, and $\hat{\gamma}_{\bar{\xi}}$ are given in Table 1. The Kronecker delta in Eq. (38) provides that if \hat{I} is not equal to those variables given in Table 1, the part it belongs to in $\hat{\mathbf{H}}_I^{CB}$ will be zero. For instance, at the first column on the right hand side of Eq. (38), variable O in Table 1 in turn is 3, 4, 7, and 8. It leads to that $\hat{\mathbf{H}}_I^{CB}$ corresponding to nodes $\hat{1}$, $\hat{2}$, $\hat{5}$, $\hat{6}$ will be zero. Matrix \mathbf{H}^{CB} of Eq. (31) is constructed in exactly the same way as for matrix $\hat{\mathbf{H}}^{CB}$, and it is specified by the following values at each node I

$$\mathbf{H}_I^{CB} = (X_I^k - X_{C_i}^k) e_{mkn} e^n [G_{\bar{\xi}}^m \delta_I^{\hat{O}} \ G_{\bar{\eta}}^m \delta_I^{\hat{P}} \ G_{\bar{\eta}}^m \delta_I^{\hat{Q}} \ G_{\bar{\zeta}}^m \delta_I^{\hat{R}} \ G_{\bar{\zeta}}^m \delta_I^{\hat{S}} \ G_{\bar{\xi}}^m \delta_I^{\hat{T}}], \quad (39a)$$

where C_i is the point located on line $\hat{1}\hat{3}$ (shown in Fig. 2) such that the following conditions are satisfied

Table 1 Variables $O, P, Q, R, S,$ and T for constant bending modes

Constant Bending Modes and Variables					
$\hat{\alpha}_{\bar{\xi}}, O$	$\hat{\alpha}_{\bar{\eta}}, P$	$\hat{\beta}_{\bar{\eta}}, Q$	$\hat{\beta}_{\bar{\zeta}}, R$	$\hat{\gamma}_{\bar{\zeta}}, S$	$\hat{\gamma}_{\bar{\xi}}, T$
3	2	5	3	2	5
4	3	6	4	3	6
7	6	7	7	6	7
8	7	8	8	7	8

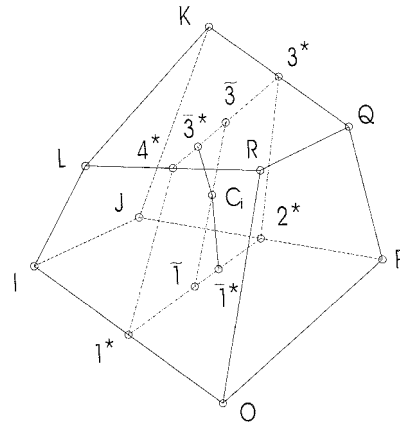


Fig. 2 Reference point C_i

$$|\mathbf{X}_{C_i} - \mathbf{X}_{\bar{1}}| |\mathbf{X}_{4^*} - \mathbf{X}_{3^*}| = |\mathbf{X}_{C_i} - \mathbf{X}_{\bar{3}}| |\mathbf{X}_{2^*} - \mathbf{X}_{1^*}|, \quad (39b)$$

$$\{\mathbf{X}_{C_i} - \mathbf{X}_{\bar{1}}\} \cdot \{\mathbf{X}_{2^*} - \mathbf{X}_{1^*}\} = 0, \quad \{\mathbf{X}_{C_i} - \mathbf{X}_{\bar{3}}\} \cdot \{\mathbf{X}_{4^*} - \mathbf{X}_{3^*}\} = 0, \quad (39c,d)$$

$$[\mathbf{X}_{1^*} \ \mathbf{X}_{2^*} \ \mathbf{X}_{3^*} \ \mathbf{X}_{4^*}] = \frac{1}{2} [\mathbf{X}_I + \mathbf{X}_O \ \mathbf{X}_J + \mathbf{X}_P \ \mathbf{X}_K + \mathbf{X}_Q \ \mathbf{X}_L + \mathbf{X}_R], \quad (39e)$$

$$[\mathbf{X}_{\bar{1}} \ \mathbf{X}_{\bar{3}}] = \frac{1}{2} [\mathbf{X}_{1^*} + \mathbf{X}_{2^*} \ \mathbf{X}_{3^*} + \mathbf{X}_{4^*}] \quad (\text{see Fig. 2}), \quad (39f)$$

variables $I, J, K, L, O, P, Q,$ and $R,$ which are used to indicate nodal points of the original hexahedral element, being given in Table 2 for each constant bending mode.

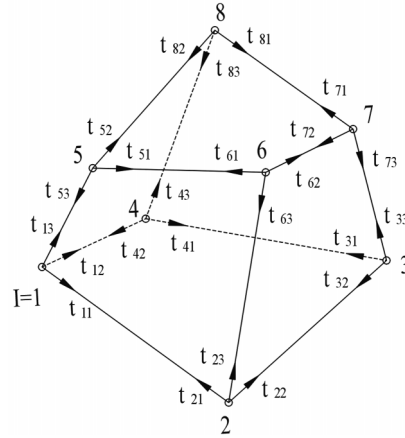
5.2.1.4 Linear bending modes

The remaining three higher order deformation modes of the associated parallelepiped are used to describe the linear bending configurations and are represented by the following three parameters

$$\hat{\mathbf{P}}^{LB} = \{\hat{\theta}_{\bar{\xi}} \ \hat{\theta}_{\bar{\eta}} \ \hat{\theta}_{\bar{\zeta}}\}^T. \quad (40)$$

Table 2 Variables $I, J, K, L, O, P, Q,$ and R for constant bending modes

Node Number	Constant Bending Mode					
	$\hat{\alpha}_{\bar{\xi}}$	$\hat{\alpha}_{\bar{\eta}}$	$\hat{\beta}_{\bar{\eta}}$	$\hat{\beta}_{\bar{\zeta}}$	$\hat{\gamma}_{\bar{\zeta}}$	$\hat{\gamma}_{\bar{\xi}}$
I	1	4	3	2	1	4
J	4	3	7	3	2	8
K	8	7	8	4	3	5
L	5	8	4	1	4	1
O	2	1	2	6	5	3
P	3	2	6	7	6	7
Q	7	6	5	8	7	6
R	6	5	1	5	8	2

Fig. 3 Designation of unit vectors t_{IM}

The linear bending mode described by $\hat{\theta}$ with a specified subscript ($\bar{\xi}$, $\bar{\eta}$, or $\bar{\zeta}$) will produce deformation causing no shear deformation on those two faces which will be intersected by the vector \mathbf{G} with the same subscript; however, the remaining four faces will undergo in-plane bending. With the deformed configuration described above, matrix $\hat{\mathbf{H}}^{LB}$ in Eq. (30) can be constructed. It is composed of eight 3×3 matrices which, for each node I of the associated parallelepiped, are in turn given as follows

$$\hat{\mathbf{H}}_I^{LB} = \hat{\xi}_I \hat{\eta}_I \hat{\zeta}_I [\mathbf{g}^{\bar{\xi}} \quad \mathbf{g}^{\bar{\eta}} \quad \mathbf{g}^{\bar{\zeta}}]. \quad (41)$$

In order to establish the relationship between vectors \mathbf{d}^{LB} and \mathbf{P}^{LB} of Eq. (31), unit vectors t_{IM} , with $M = 1, 2, 3$, are constructed at every node I of the original hexahedral element and designated as shown on Fig. 3. The part of matrix \mathbf{H}^{LB} of Eq. (31) related to node I of the original hexahedral element is then given by the following expression

$$\mathbf{H}_I^{LB} = [\Theta_{I\xi}^1 \mathbf{t}_I^1 \quad \Theta_{I\eta}^2 \mathbf{t}_I^2 \quad \Theta_{I\zeta}^3 \mathbf{t}_I^3], \quad \Theta_{I\#}^k = \frac{\mathbf{t}_{I\#} \bullet \mathbf{t}_{I\#}^k}{\mathbf{t}_I^k \bullet \mathbf{t}_{I\#}}, \quad \mathbf{t}_{I\#} = N_I^j \hat{\xi}_j \hat{\eta}_j \hat{\zeta}_j \mathbf{g}^{\#}, \quad \# = \xi, \eta, \zeta, \quad (42a,b,c)$$

The coefficient $\Theta_{I\#}^k$ is used to obtain a condition such that the projection of vectors $\Theta_{I\#}^k \mathbf{t}_I^k$ on the direction of vector $\mathbf{t}_{I\#}$ is equal to the length of vector $\mathbf{t}_{I\#}$. In this sense, the magnitude of the parameters describing three linear bending modes of the associated parallelepiped are the same as that of the original hexahedral element.

5.2.2 Displacement extrapolation matrix

With the use of Eqs. (30, 31) and assuming that the deformation modes of the original hexahedral element are identical as those for the associated parallelepiped, displacement extrapolation matrix of Eq. (29) can be established. The result is given as follows

$$\Psi = [\hat{\mathbf{C}} \quad \hat{\mathbf{H}}^{LS} \quad \hat{\mathbf{H}}^{CB} \quad \hat{\mathbf{H}}^{LB}] [\mathbf{C} \quad \mathbf{H}^{LS} \quad \mathbf{H}^{CB} \quad \mathbf{H}^{LB}]^{-1}. \quad (43)$$

Note that the matrix needs to be inverted on element level is of dimension 24×24 . From saving computational efforts point of view, this is perhaps the disadvantage of the proposed approach. However, in the analysis of a system modeled by a large number of elements, the time spent on the formulation of each element level is typically a small portion of the total computational time. Therefore, the increased effort in the formulation of the element stiffness matrix is not necessarily a drawback of this approach, particularly that a payoff in the form of consistently increased accuracy is achieved. Many attempts have also been investigated to see if other forms of the displacement extrapolation technique could be used to further improve its behaviour and to avoid the inversion of 24 by 24 matrix. For example, if the concept employed in Eq. (28a) is adopted to construct the displacement extrapolation matrix, only one 8 by 8 matrix has to be inverted on each element level. Comparisons based on the solutions obtained from different approaches have demonstrated that the results obtained by means of the displacement extrapolation techniques proposed in Chen and Stolarski 1998 is very accurate.

5.3 Element stiffness matrix

Substitution of Eq. (29) into Eq. (28a) leads to the assumed strain field for the original hexahedral element expressed in terms of its own nodal displacements

$$\bar{\boldsymbol{\varepsilon}}_I^* = \bar{\mathbf{B}}_I^* \Psi \mathbf{d} = \bar{\mathbf{B}}_I^* \mathbf{d}, \quad (44)$$

where $\bar{\mathbf{B}}_I^*$ is the assumed strain operator at node I of the original hexahedral element. Finally, the assumed strain field of the original hexahedral element is given by

$$\boldsymbol{\varepsilon}^* = \Gamma_{\varepsilon} \mathbf{N}^I \bar{\boldsymbol{\varepsilon}}_I^* = \Gamma_{\varepsilon} \bar{\mathbf{B}}^* \mathbf{d} = \mathbf{B}^* \mathbf{d}, \quad \mathbf{N}^I = \frac{1}{8} (1 + \xi_I \xi) (1 + \eta_I \eta) (1 + \zeta_I \zeta). \quad (45a,b)$$

In the above equations, $\bar{\mathbf{B}}^*$ is the assumed strain operator expressed in terms of the $(\bar{\xi}, \bar{\eta}, \bar{\zeta})$ frame whereas \mathbf{B}^* is that expressed with respect to the global fixed frame. With the strain-displacement operator $\bar{\mathbf{B}}^*$ or \mathbf{B}^* of the original hexahedral element determined and by means of tensor algebra, the element stiffness matrix can be expressed as

$$\mathbf{K}_e^* = \int_{\Omega_e} (\bar{\mathbf{B}}^*)^T (\boldsymbol{\Gamma}_\varepsilon^T \mathbf{D} \boldsymbol{\Gamma}_\varepsilon) \bar{\mathbf{B}}^* d\Omega_e \left\{ \begin{array}{l} = \int_{\Omega_e} (\bar{\mathbf{B}}^*)^T \mathbf{D} \bar{\mathbf{B}}^* d\Omega_e, \text{ for regular elements,} \\ \cong \int_{\Omega_e} (\bar{\mathbf{B}}^*)^T \mathbf{D} \bar{\mathbf{B}}^* d\Omega_e, \text{ for skewed elements,} \end{array} \right. \quad (46)$$

where Ω_e is the element domain and \mathbf{D} is the matrix of material elastic constants.

The procedure of formulating the strain-displacement operator $\bar{\mathbf{B}}^*$ for the associated parallelogram in the natural coordinate system is straightforward. And as shown in Eq. (46), $\boldsymbol{\Gamma}_\varepsilon^T \mathbf{D} \boldsymbol{\Gamma}_\varepsilon = \mathbf{D}$ is used for both regular and skewed elements. However, it is noted that $\boldsymbol{\Gamma}_\varepsilon^T \mathbf{D} \boldsymbol{\Gamma}_\varepsilon = \mathbf{D}$ is valid for any regular element, and is an approximation for skewed elements. It implies that basis $(\bar{\mathbf{g}}_{\bar{\xi}}, \bar{\mathbf{g}}_{\bar{\eta}}, \bar{\mathbf{g}}_{\bar{\zeta}})$ for a skewed element is assumed to be orthogonal. Although this assumption is somewhat less nature, numerical simulation has demonstrated that performance of the proposed element is excellent in both bending and membrane problems even when severely skewed elements are used.

Note that the assumed strain-displacement operator $\bar{\mathbf{B}}^*$ in Eq. (46) is expressed in the $(\bar{\xi}, \bar{\eta}, \bar{\zeta})$ frame, and is a matrix of polynomials with respect to the isoparametric coordinates. In addition, the Jacobian of isoparametric mapping is also a polynomial; as a result, the expression defining the element stiffness matrix can be integrated analytically. Although it is true, numerical integration is still used to evaluate the element stiffness matrix to avoid lengthy derivative of the explicit expression of the element stiffness matrix.

6. Numerical simulations and discussions

Performance of the present mixed eight-node hexahedral elements is evaluated based on the analysis of benchmark problems frequently used in the literature. The elements used in this comparison are labeled as follows:

H8: the standard eight-node isoparametric hexahedral element.

HM9: the non-conforming eight-node hexahedral element (Taylor *et al.* 1976).

PT18 β : the assumed stress hexahedral element (Pian and Tong 1986).

HEX8RX: the eight-node hexahedral element with rotational DOFs (Yunus *et al.* 1991).

HBR2: the eight-node hexahedral element with rotational DOFs (Sze *et al.* 1996).

SS18 β : the assumed stress hexahedral element (Sze and Ghali 1993).

MIXED: the mixed bi-linear shell element (Simo *et al.* 1989).

B8-24/15/9P: the mixed eight-node hexahedral element (Weissman 1996).

HMOD1 and **HMOD2**: the assumed strain eight-node hexahedral elements (Chen and Stolarski 1998).

M18 β : the assumed stress hexahedral element (Yeo and Lee 1997).

ANS $\gamma\epsilon$ and **ANS $\gamma\epsilon$ -HS**: the solid-shell elements (Sze and Yao 2000).

HMIX1: the proposed mixed eight-node hexahedral element.

6.1 Cantilever beam under pure bending load

The performance of the present three-dimensional models under pure bending conditions and the effect of mesh distortion on the accuracy is studied by using the two-element cantilever beam as

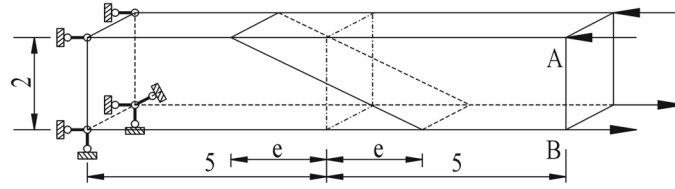


Fig. 4 Cantilever beam under pure bending load

Table 3 Normalized displacements for the cantilever beam under pure bending load

Parameter	$\nu = 0.25$ (plane stress and plane strain)						$\nu = 0.4999$ (plane stress and plane strain)						
	e	u_A	v_A	w_A	u_B	v_B	w_B	u_A	v_A	w_A	u_B	v_B	w_B
0	1.00	1.00	1.00	1.00	1.00	1.00	1.00	1.00	1.00	1.00	1.00	1.00	1.00
1	1.00	1.00	1.00	1.00	1.00	1.00	1.00	1.00	1.00	1.00	1.00	1.00	1.00
2	1.00	1.00	1.00	1.00	1.00	1.00	1.00	1.00	1.00	1.00	1.00	1.00	1.00
3	1.00	1.00	1.00	1.00	1.00	1.00	1.00	1.00	1.00	1.00	1.00	1.00	1.00
4	1.00	1.00	1.00	1.00	1.00	1.00	1.00	1.00	1.00	1.00	1.00	1.00	1.00

shown in Fig. 4. This is perhaps the most critical problem used in testing element's bending properties under the effect of mesh distortion. The cantilever beam of dimension $10 \times 2 \times 1$ is subjected to an end moment. The interelement boundary is then gradually rotated with respect to the direction of bending (a distance e on the top and bottom surfaces) to skew the mesh. For the mesh layouts stated above, Poisson's ratio $\nu = 0.25$ and $\nu = 0.4999$ are considered for plane stress state. In addition, analysis of this problem under the condition of plane strain is also performed by suppressing all the nodal displacements in the direction of applied bending moment. The displacements at points A and B are normalized with respect to the theoretical solution based on the beam theory. These normalized displacements are listed in Table 3 for the proposed **HMIX1** element. It is interesting to note that the predictions (including all displacement components and stress components) of **HMIX1** element are identical to the theoretical solutions even when $e = 4$. It provides a good indication that the mixed formulation proposed in this work can lead to an excellent bending behavior for the low-order eight-node hexahedral element. The **B8-15P** and **B8-24P** elements were tested for this problem under the state of plane strain with Poisson's ratio $\nu = 0$ and $\nu = 0.4999$. The lower edge vertical displacements were reported, and numerical results show that, compare with the theoretical solution, more than 30% of deviation is observed for both $\nu = 0$ and $\nu = 0.4999$ when parameter $e \geq 1$.

In order to verify if the proposed **HMIX1** element is invariant, the cantilever beam is analyzed by rotating the beam an arbitrary angle in the direction of the applied end moment. All results produced for all cases are identical to the theoretical solution demonstrating that the proposed element is invariant. Nodal ordering are also rearranged to change the direction of the natural coordinate of the element, and the test confirms that the proposed mixed element is invariant to node numbering.

6.2 MacNeal's elongated beam

This elongated cantilever beam of dimension $6 \times 0.2 \times 0.1$ is presented by MacNeal and Harder 1985. The beam is modelled using three 1×6 meshes consisting of rectangular prism, trapezoidal prism, and parallelepiped elements, as shown in Fig. 5. This beam is subjected to either an in-plane or an out-of-plane end shear load. This problem is used to test the locking problem, which is due to the use of high aspect ratio and irregular meshes. The normalized results are listed in Table 4. For this problem, **HMOD1**, **NMOD2**, and the proposed **HMIX1** elements exhibit excellent performance for all loading cases and mesh layouts. They are slightly outperform **HEX8RX** and **HBR2** elements. For a trapezoidal shape of the elements, severe locking phenomenon plagues **H8**, **HM9**, **PT18 β** , and **SS18 β** elements. Furthermore, unsatisfactory performance is noted for a parallelepiped shape of the elements. For the case when the beam is modeled by parallelepiped elements and is

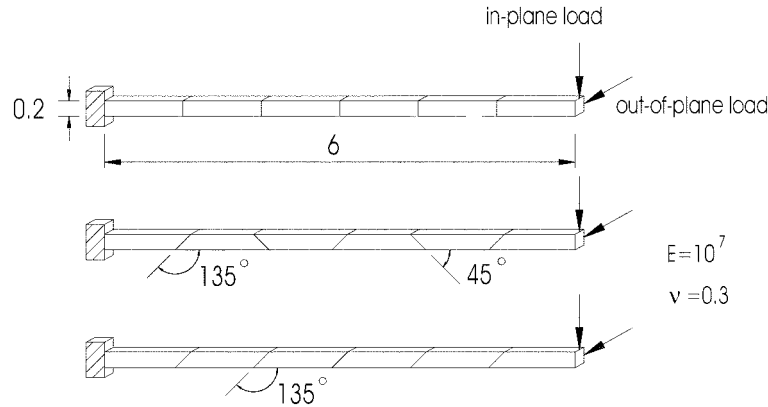


Fig. 5 MacNeal's elongated beam

Table 4 Normalized displacements at the free end of MacNeal's elongated beam

Element Model	In-Plane Load			Out-of-Plane Load		
	Rectangular	Trapezoidal	Parallelepiped	Rectangular	Trapezoidal	Parallelepiped
H8	0.093	0.026	0.032	0.025	0.010	0.014
HM9	0.978	0.047	0.624	0.973	0.030	0.528
PT18β	0.981	0.047	0.625	0.981	0.031	0.587
HEX8RX	0.988	0.863	0.921	0.983	0.943	0.969
SS18β	0.981	0.047	0.625	0.981	0.031	0.587
HBR2	0.978	0.915	0.938	0.980	0.927	0.960
HMOD1	0.981	0.981	0.981	0.981	0.972	0.739
HMOD2	0.981	0.981	0.980	0.981	0.979	0.731
M18β	0.992	0.338	0.943	n.a.	n.a.	n.a.
ANS$\gamma\epsilon$	0.904	0.912	n.a.	n.a.	n.a.	n.a.
ANS$\gamma\epsilon$-HS	0.993	1.001	n.a.	n.a.	n.a.	n.a.
HMIX1	0.981	0.982	0.984	0.981	0.980	0.983

loaded by an out-of-plane end shear force, the proposed **HMIX1** element can still provide excellent accuracy. Prediction of the **M18 β** element reveals that trapezoidal locking phenomenon is noticeable. Both **ANS $\gamma\epsilon$** and **ANS $\gamma\epsilon$ -HS** elements are able to overcome this problem.

6.3 Curved cantilever beam

This clamped curved cantilever beam loaded with either an unit in-plane or an unit out-of-plane load at the free end, as shown in Fig. 6, is also presented by MacNeal and Harder 1985. The beam is modelled using 1×6 equispaced mesh. The out-of-plane load is used to test the element's performance under a combination of bending and torsion. The geometric parameters are inner radius $R_I = 4.12$, outer radius $R_O = 4.32$, and thickness $t = 0.1$. The reference tip displacements in the direction of loading for the plane stress curved cantilever beam are 0.08734 and 0.5022 for the unit

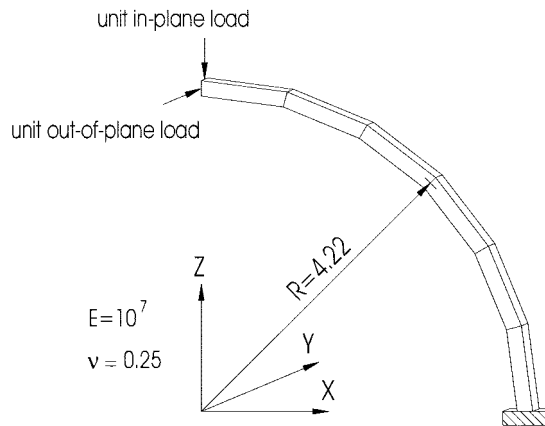


Fig. 6 Curved cantilever beam

Table 5 Normalized displacements in the direction of loading for curved and twisted cantilever beams

Element Model	Curved Cantilever Beam		Twisted Cantilever Beam	
	in-plane load	out-of-plane load	in-plane load	out-of-plane load
H8	0.073	0.231	0.208	0.108
HM9	0.876	0.819	0.995	0.989
PT18β	0.877	0.846	1.001	0.992
HEX8RX	0.997	0.890	1.001	0.999
SS18β	0.877	0.846	1.001	0.992
HBR2	0.992	0.863	0.997	0.997
HMOD1	1.013	0.943	0.999	1.001
HMOD2	1.012	0.943	0.999	1.001
ANS$\gamma\epsilon$	n.a.	n.a.	0.945	0.887
ANS$\gamma\epsilon$-HS	n.a.	n.a.	1.001	0.990
HMIX1	1.013	0.942	0.999	1.001

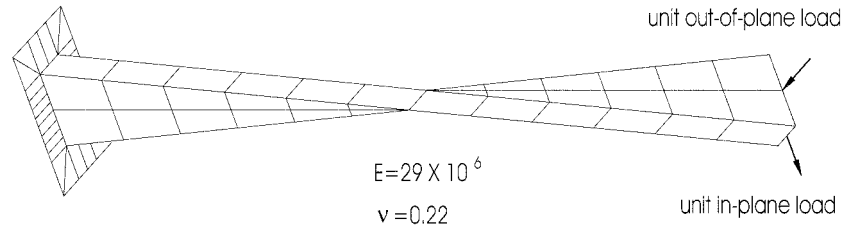


Fig. 7 Twisted cantilever beam

in-plane load and the unit out-of-plane load, respectively. The results, normalized with respect to the analytical solutions, are summarized in Table 5. It is shown that prediction of the proposed **HMIX1** element is almost identical to **HMOD1** and **HMOD2** elements. Their predictions are superior to other elements cited here for comparison. For the case of out-of-plane load when torsion is involved, **HMOD1**, **HMOD2**, and the proposed **HMIX1** elements can still yield very satisfactory accuracy.

6.4 Twisted cantilever beam

The beam twisted by the angle of 90° from the fixed end to the free end is also suggested by MacNeal and Harder 1985. It is used to test the element performance due to the use of warped configuration. The twisted beam is modelled by using 2×12 mesh and loaded with either an unit in-plane or an unit out-of-plane load as shown in Fig. 7. The geometric parameters are length $L = 12$, depth $D = 1.1$, and thickness $t = 0.32$. The analytical tip displacements in the direction of loading are 0.005424 and 0.001754 for the unit in-plane and the unit out-of-plane loads, respectively. The normalized results are reported in Table 5. The results show that predictions of all elements except the **H8** element exhibit excellent accuracy.

6.5 Pinched circular ring

A circular ring with rectangular cross section $t \times t$ and radius $R = 1$, as shown in Fig. 8, is

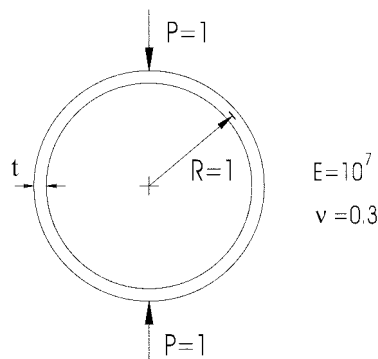


Fig. 8 Pinched circular ring

Table 6 Normalized displacements in the direction of loading of the pinched circular ring

Element Model	$R/t = 60$			$R/t = 100$			$R/t = 500$		
	Mesh layout			Mesh layout			Mesh layout		
	1×4	1×8	1×16	1×4	1×8	1×16	1×4	1×8	1×16
H8	0.004	0.018	0.068	0.002	0.073	0.073	0.000	0.000	0.000
HM9	0.177	0.908	0.991	0.007	0.822	0.822	0.003	0.187	0.925
PT18β	0.178	0.909	0.992	0.026	0.989	0.989	0.003	0.187	0.925
SS18β	0.853	0.909	0.992	0.852	0.967	0.992	0.852	0.967	0.992
HMOD1	0.952	0.988	0.997	0.952	0.988	0.997	0.952	0.988	0.997
HMOD2	0.952	0.988	0.997	0.952	0.988	0.997	0.952	0.988	0.997
HMIX1	0.952	0.988	0.997	0.952	0.988	0.997	0.952	0.988	0.997

compressed by two unit loads acting along a diameter. This problem is analyzed under the condition of plane stress situation. Owing to symmetry, only one-quarter of the circular ring is modelled by using 1×4 , 1×8 , and 1×16 equispaced meshes. For this problem, $t = 1/60$, $1/100$, and $1/500$ are used to test the locking problem due to the use of high aspect ratio and coarse meshes. The displacements in the direction of loading are normalized with respect to the theoretical solutions, and listed in Table 6. The **HMOD1**, **HMOD2**, and the proposed **HMIX1** elements exhibit excellent performance for all three thicknesses. It also shows that they are insensitive to the change of R/t ratio. Their predictions are slightly superior to the **SS18 β** element. **HM9** and **PT18 β** elements show severe locking problem for large R/t ratio and coarse meshes. The **H8** element locks severely for all cases.

6.6 Simply supported square plate

A simply supported square plate of length $L = 10$ and thickness $t = 0.1$ is loaded by an uniform distributed loading of intensity 1. Owing to symmetry, only one-quarter of the plate is modelled by using 2×2 , 3×3 , and 4×4 evenly divided meshes as shown in Fig. 9. The vertical displacements at the centre of the plate are normalized with respect to the theoretical deflection, and listed in Table 7.

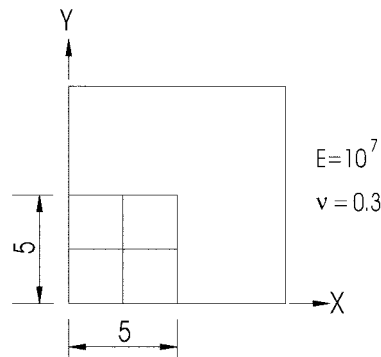


Fig. 9 Simply supported square plate

Table 7 Normalized displacements at the center of simply supported square plate and clamped circular plate

Element Model	Simply Supported Square Plate			Clamped Circular Plate		
	Mesh layout			Number of element		
	2×2	3×3	4×4	3	12	48
H8	0.009	0.020	0.035	0.006	0.020	0.072
HM9	0.101	0.466	0.737	0.116	0.579	0.926
PT18β	0.990	0.997	0.999	0.517	0.869	0.983
HEX8RX	0.981	n.a.	1.005	0.252	0.850	0.967
SS18β	1.038	1.017	1.011	0.807	0.899	0.983
HBR2	0.793	n.a.	0.999	0.210	0.832	0.962
HMOD1	0.990	0.997	0.999	0.667	0.907	0.974
HMOD2	0.990	0.997	0.999	0.670	0.917	0.972
HMIX1	0.990	0.997	0.999	0.596	0.838	0.909

Results obtained by **PT18 β** , **HMOD1**, **HMOD2**, and the proposed **HMIX1** elements are almost identical, and they are slightly superior to the results due to the **SS18 β** element. The **HBR2** element produced unsatisfactory prediction for the mesh of 2×2 . Although, eventually, the prediction of the **HM9** element tends to converge to solution with the refinement of the mesh, unsatisfactory performance still exists for the mesh of 4×4 .

6.7 Clamped circular plate loaded by central point load

Displacement field due to concentrated force applied to a plate allowing for shear deformation is singular. Thus, numerical calculations concerning such cases should be viewed with proper caution. The results reported here serve only the purpose of comparison with other results obtained under identical conditions.

A clamped circular plate with radius $R = 5$ and thickness $t = 0.1$ is loaded by an unit central point load. Owing to symmetry, only one-quarter of the circular plate is analyzed by using three meshes of 3, 12, and 48 elements as shown in Fig. 10. The central displacements in the direction of the unit point load are normalized with respect to the theoretical solution 5.4312, and are listed in Table 7. Due to the use of shear scaling factors, the **SS18 β** element exhibits very good behavior for irregular

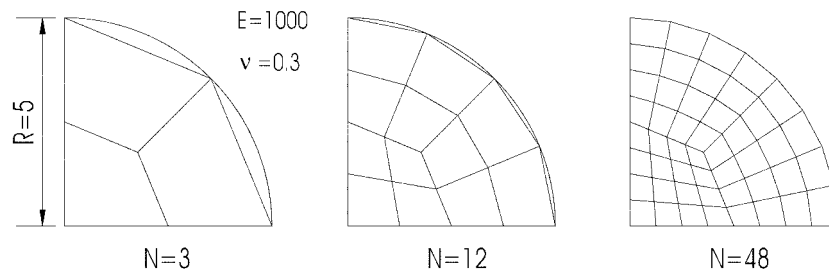


Fig. 10 Clamped circular plate under central point load

and coarse meshes. It is mainly related to the fact that undesirable shear strain caused by the use of distorted meshes is scaled down by using the shear scaling factors. Numerical performance of **PT18 β** , **HMOD1**, and **HMOD2** elements are similar for this problem. Their predictions are superior to that of the proposed **HMIX1** element. Although, eventually, predictions of **HEX8RX** and **HBR2** elements converge to satisfactory solution with the refinement of the mesh, their performance for coarse mesh using 3 elements is unsatisfactory. However, it is noted that for small number of element (3,12) the boundary condition will be fixed along piecewise straight edges and that is different from the clamped continue circle edge. As a result, a stiffened response should be expected.

6.8 Hemispherical shell under alternating point load

A hemispherical shell with a 18° hole at the top of the shell is subjected to two pairs of orthogonal and opposite forces (one pair in inward diameter direction, the other pair in outward diameter direction). Owing to symmetry, only one-quarter of the shell is modelled by using 2×2 , 4×4 , 8×8 , and 12×12 meshes as illustrated in Fig. 11. The geometric parameters are radius $R=10$ and thickness $t=0.04$. The displacements in the direction of loading at point A are normalized with respect to 0.094 (MacNeal and Harder 1985). These normalized results are listed in Table 8. Although, the proposed **HMIX1** element's performance is inferior to that due to **SS18 β** , **MIXED**, **HMOD1**, **HMOD2**, **ANS $\gamma\epsilon$** , and **ANS $\gamma\epsilon$ -HS** elements for coarse meshes of 2×2 and 4×4 , it is capable of yielding satisfactory solutions with the use of 8×8 mesh. Although the predictions of the **PT18 β** element are inferior to that of **SS18 β** , **HMOD1**, **HMOD2**, **ANS $\gamma\epsilon$** , **ANS $\gamma\epsilon$ -HS**, and the proposed **HMIX1** elements, it eventually converges to the reference solution for 12×12 mesh. It seem fair to note here that the meshes used here consist of flat elements and that for small number of elements (2×2 , 4×4) the model is geometrically significantly different from the sphere. As a result, a significantly different behavior should be expected even if the problem of piecewise flat surface is solved exactly.

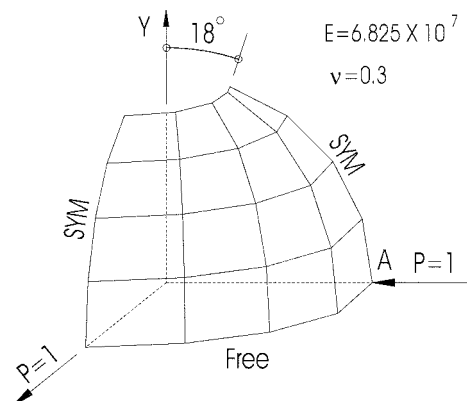


Fig. 11 Hemispherical shell under alternating point load

Table 8 Normalized displacements at point A in the direction of loading for hemispherical shell and Scordelis-Lo roof

Element Model	Hemispherical Shell				Scordelis-Lo Roof		
	Mesh layout				Mesh layout		
	2 × 2	4 × 4	8 × 8	12 × 12	2 × 2	4 × 4	8 × 8
H8	0.000	0.001	0.003	0.006	0.025	0.062	0.121
HM9	0.000	0.010	0.163	0.493	0.139	0.542	0.947
PT18β	0.000	0.041	0.742	0.957	1.331	1.028	1.002
SS18β	0.721	1.050	1.007	0.998	1.459	1.061	1.007
MIXED	0.919	1.004	0.998	n.a.	1.450	1.083	1.015
HMOD1	1.106	0.986	1.008	0.998	1.421	1.037	0.987
HMOD2	1.232	1.073	1.008	0.998	1.421	1.037	0.987
ANSγε	1.100	1.042	0.997	n.a.	1.214	0.938	0.962
ANSγε-HS	1.184	1.062	1.006	n.a.	1.428	1.044	0.995
HMIX1	0.039	0.543	0.981	0.991	1.351	1.042	0.995

6.9 Scordelis-Lo roof

The Scordelis-Lo problem is loaded by gravity loading of intensity 90 unit per midsurface area. This is a membrane dominated problem to test the ability of the element to model complex states of membrane response. Owing to symmetry, only one-quarter of the shell is modelled by using 2×2 , 4×4 , and 8×8 meshes as indicated in Fig. 12. The geometric parameters are Length of the shell $L = 50$, thickness $t = 0.25$, radius $R = 25$, and angle $\phi = 40^\circ$. For the displacement in the direction of gravity loading at point A on the midsurface, two different reference solutions 0.3024 and 0.3086 (MacNeal and Harder 1985) are commonly used in the comparison. In this work, the computed displacements at the point A are normalized with respect to the value of 0.3086 to make it comparable with the results of others. These normalized results are listed in Table 8. For this problem, **PT18β**, **SS18β**, **MIXED**, **HMOD1**, **HMOD2**, **ANSγε-HS**, and the proposed **HMIX1** elements yield similar performance. For the mesh 2×2 , all the above mentioned elements exhibit excessively soft behavior. This is probably because of inadequate representative of geometry by so

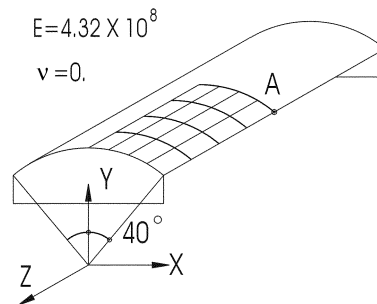


Fig. 12 Scordelis-Lo roof

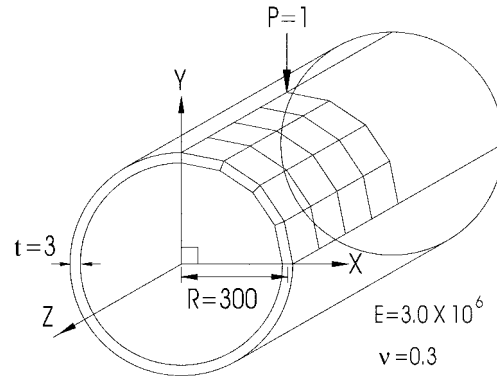


Fig. 13 Pinched cylinder with end diaphragms

Table 9 Normalized displacements at the loaded point in the direction of loading for the pinched cylinder with end diaphragms

Element Model	Mesh layout			
	2×2	4×4	8×8	16×16
MIXED	----	0.399	0.763	0.935
B8-24/15/9P	----	0.100	0.400	0.740
HMOD1	0.044	0.400	0.765	0.937
ANSγe	n.a.	0.357	0.675	n.a.
ANSγe-HS	n.a.	0.401	0.766	n.a.
HMIX1	0.043	0.398	0.764	0.937

few flat elements. The **HM9** element yields improved performance with the refinement of the mesh while it locks for the coarse meshes.

6.10 Pinched cylinder with end diaphragms

A hollow cylinder with rigid diaphragms at both ends is loaded by a pair of pinched vertical forces at the middle section of the cylinder. Owing to symmetry, only one octant of the cylinder is modeled by using 2×2 , 4×4 , 8×8 , and 16×16 meshes as illustrated in Fig. 13. The geometric parameters are length $L = 600$, radius $R = 300$, and thickness $t = 3$. The displacements at the loaded point in the direction of loading are normalized with respect to the analytical solution of 1.82488×10^{-5} and listed in Table 9. The results show that predictions of **MIXED**, **HMOD1**, **ANS γ e-HS**, and the proposed **HMIX1** elements are almost the same for this problem. They are superior to the performance of **B8-24/15/9p** elements. It is noted that results due to **B8-24/15/9P** elements are quoted from the Fig. 15 given in Weissman 1996.

6.11 Thick-walled cylinder

A thick-walled cylinder has been chosen to provide an additional test whether the element locks

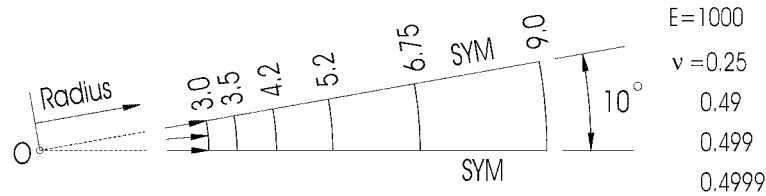


Fig. 14 Thick-walled cylinder under internal pressure

Table 10 Normalized displacements in the radial direction at the inner surface of the thick cylinder

Element Model	Poisson's Ratio			
	$\nu = 0.25$	$\nu = 0.49$	$\nu = 0.499$	$\nu = 0.4999$
H8	0.986	0.845	0.359	0.053
HM9	0.991	0.986	0.986	0.986
PT18β	0.991	0.986	0.986	0.986
SS18β	0.991	0.986	0.986	0.986
HMOD1	0.969	0.966	0.966	0.966
HMOD2	0.969	0.966	0.966	0.966
ANS$\gamma\epsilon$	n.a.	0.845	0.053	n.a.
ANS$\gamma\epsilon$-HS	n.a.	0.986	0.990	n.a.
HMIX1	0.969	0.966	0.966	0.966

for nearly incompressible material. This thick walled cylinder is subjected to unit internal pressure and is considered to be at the plane strain state. The geometric parameters are inner radius $R_I = 3$ and outer radius $R_O = 9$. Owing to axial symmetry, only a wedge of the thick-wall cylinder with unit thickness is analyzed for the mesh layout shown in Fig. 14. In addition to the symmetric boundary conditions along the radial directions of the wedge, displacements along the axial direction are fixed on the top and bottom surfaces of the wedge to model the plane strain state. The normalized radial displacements at the inner wall are computed and given in Table 10. All elements except the **H8** and **ANS $\gamma\epsilon$** elements are insensitive to the value of Poisson's ratio even very close to incompressibility for this standard plane strain problem. Performance of **HMOD1**, **HMOD2**, and the proposed **HMIX1** elements are almost identical. Prediction of the **ANS $\gamma\epsilon$ -HS** element is superior to the **HMIX1** element.

7. Conclusions

A mixed formulation capable of providing highly accurate bending properties for the low-order eight-node hexahedral element is introduced. The so-called shear locking and membrane locking problems have been successfully overcome. In particular, in the case of three-dimensional straight cantilever beam under pure bending load, the theoretical solution for displacements and stresses is obtained even when severely distorted meshes are used for nearly incompressible materials. Numerical evaluation has supported that the mixed eight-node hexahedral element is suitable for

structural analysis problems such as spacial beams, plates, and shells as well as general three-dimensional elasticity problems.

From the implementation point of view, the formulation of the element is quite simple. With three independent fields selected and use of Hu-Washizu variational principle, the assumed strain field at the nodal points of the associated parallelepiped can be obtained analytically and explicitly. The strain and displacement extrapolations are then performed to evaluate the assumed strain field at the nodal points of the original hexahedral. Finally, by simply using standard trilinear functions, the assumed strain field over the entire domain of the original hexahedral element is established. The expression defining the element stiffness matrix can be integrated analytically without any use of numerical integration. However, inversion of one 24 by 24 matrix is needed to construct the displacement extrapolation matrix. As mentioned in Chen and Stolarski 1998, element stiffness matrices of **HMOD1** and **HMOD2** can also be obtained analytically. Although numerical results produced by **HMOD1** and **HMOD2** elements are almost identical to that given by the present **HMIX1** element, eight 6 by 6 matrices and two 24 by 24 matrices have to be inverted during the course of formulating **HMOD1** and **HMOD2** elements. By using the proposed formulation, computational effort on element level is reduced substantially without scarifying the element's performance.

In this paper, comparison has been made with some other well-known formulations including the same hexahedral elements with drilling degrees of freedom, other mixed formulations, solid-shell elements, as well as four-node shell elements. In all cases, it reveals a very competitive behavior of the proposed element in terms of element's accuracy. The proposed mixed eight-node hexahedral element passes the patch test only when the element with a shape of regular or parallelepiped. Practically, in the finite element analysis, irregular or distorted elements are inevitable generated in mesh layout, and the mesh refinement process usually leads to that the initially irregular or skewed shapes of the hexahedral elements will gradually approach parallelepiped shapes. From this point of view, a hexahedral element that is able to pass the patch test for the parallelepiped shape is important and useful for practical applications. Tests from solving benchmark problems have demonstrated that the proposed element is capable of producing convergent and reliable solutions, and its convergence characteristics are very satisfactory.

References

- Belytschko, T. and Bindeman, L.P. (1993), "Assumed strain stabilization of the eight node hexahedral element", *Comp. Meth. Appl. Mech. Eng.*, **105**, 225-260.
- Cao, Y.P., Hu, N., Lu, J., Fukunaga, H. and Yao, Z.H. (2002), "A 3D brick element based on Hu-Washizu variational principle for mesh distortion", *Int. J. Num. Meth. Eng.*, **53**, 2529-2548.
- Chandra, S. and Prathap, G. (1989), "A field-consistent formulation for the eight-noded solid finite element", *Comp. Struct.*, **33**, 345-355.
- Chen, W.-J. and Cheung, Y.K. (1992), "Three-dimensional 8-node and 20-node refined hybrid isoparametric elements", *Int. J. Num. Meth. Eng.*, **35**, 1871-1889.
- Chen, Y.-I and Stolarski, H.K. (1998), "Extrapolated fields in the formulation of the assumed strain elements. Part 1: Three-dimensional problems", *Comp. Meth. Appl. Mech. Eng.*, **154**, 1-29.
- Chen, Y.-I (2002), "Mixed formulation based on Hu-Washizu principle and concept of field extrapolation for the four-node quadrilateral element", *Int. J. Num. Meth. Eng.* (submitted).
- Cheung, Y.K. and Chen, W.-J. (1988), "Isoparametric hybrid hexahedral elements for three dimensional stress analysis", *Int. J. Num. Meth. Eng.*, **26**, 677-693.

- Flanagan, D.P. and Belytschko, T. (1981), "A uniform strain hexahedron and quadrilateral with orthogonal hourglass control", *Int. J. Num. Meth. Eng.*, **17**, 679-706.
- Ibrahimbegovic, A. and Wilson, E.L. (1991), "Thick shell and solid finite elements with independent rotation fields", *Int. J. Num. Meth. Eng.*, **31**, 1393-1414.
- MacNeal, R.H. and Harder, R.L. (1985), "A proposed standard set of problems to test finite element accuracy", *Finite Elements Anal. Des.*, **1**, 3-20.
- MacNeal, R.H. (1987), "A theorem regarding the locking of tapered four-noded membrane elements", *Int. J. Num. Meth. Eng.*, **24**, 1793-1799.
- Pian, T.H.H. (1964), "Derivation of element stiffness matrices by assumed stress distributions", *AIAA J.*, **2**, 1333-1336.
- Pian, T.H.H. and Chen, D.P. (1983), "On the suppression of zero energy deformation modes", *Int. J. Num. Meth. Eng.*, **19**, 1741-1752.
- Pian, T.H.H. and Sumihara, K. (1984), "Rational approach for assumed stress finite elements", *Int. J. Num. Meth. Eng.*, **20**, 1685-1695.
- Pian, T.H.H. and Tong, P. (1986), "Relations between incompatible displacement model and hybrid stress model", *Int. J. Num. Meth. Eng.*, **22**, 173-181.
- Simo, J.C., Fox, D.D. and Rifai, M.S. (1989), "On a stress resultant geometrically exact shell model. Part II: The linear theory; computational aspects", *Comp. Meth. Appl. Mech. Eng.*, **73**, 53-92.
- Sze, K.Y. and Ghali, A. (1993), "Hybrid hexahedral element for solids, plates, shells and beams by selective scaling", *Int. J. Num. Meth. Eng.*, **36**, 1519-1540.
- Sze, K.Y., Soh, A.K. and Sim, Y.S. (1996), "Solid elements with rotational DOFs by explicit hybrid stabilization", *Int. J. Num. Meth. Eng.*, **39**, 2987-3005.
- Sze, K.Y. and Yao, L.Q. (2000), "A hybrid stress ANS solid-shell element and its generalization for smart structure modelling. Part I-solid-shell element formulation", *Int. J. Num. Meth. Eng.*, **48**, 545-564.
- Taylor, R.L., Beresford, P.J. and Wilson, E.L. (1976), "A nonconforming element for stress analysis", *Int. J. Num. Meth. Eng.*, **10**, 1211-1219.
- Wang, X.-J. and Belytschko, T. (1987), "An efficient flexurally superconvergent hexahedral element", *Eng. Comp.*, **4**, 281-288.
- Weissman, S.L. (1996), "High-accuracy low-order three-dimensional brick elements", *Int. J. Num. Meth. Eng.*, **39**, 2337-2361.
- Wilson, E.L., Taylor, R.L., Doherty, W.P. and Ghaboussi, J. (1973), "Incompatible displacement models", in: S.J. Fenves *et al.*, eds., *Numerical and Computer Methods in Structural Mechanics*, Academic Press, New York, pp.43-57.
- Yeo, S.T. and Lee, B.C. (1997), "New stress assumption for hybrid stress elements and refined four-node plane and eight node brick elements", *Int. J. Num. Meth. Eng.*, **40**, 2933-2952.
- Yunus, S.M., Pawlak, T.P. and Cook, R.D. (1991), "Solid elements with rotational degrees of freedom: Part 1 - hexahedral elements", *Int. J. Num. Meth. Eng.*, **31**, 573-592.